ACS APPLIED NANO MATERIALS

www.acsanm.org
Article

A Hexanuclear Gadolinium(III)-Based Nanoprobe for Magnetic Resonance Imaging of Tumor Apoptosis

Yufan Wu,[⊥] Shuo Zhao,[⊥] Ye Xu, Chaojie Tang, Yujie Feng, Mianmian Zhang, Hong Yang, Yunsheng Ma,* Yuehua Li,* and Wu Wang*

Cite This: ACS Appl. Nano Mater. 2024, 7, 9020−9030
Read Online

ABSTRACT: Magnetic resonance imaging (MRI) is instrumental in the noninvasive evaluation of tumor tissues in patients subjected to chemotherapy, thereby yielding essential diagnostic data crucial for the prognosis of tumors and the formulation of therapeutic strategies. Currently, commercially available MRI contrast agents (CAs) predominantly consist of mononuclear gadolinium(III) complexes. Because there is only one Gd(III) atom per molecule, these CAs often require administration in high doses to achieve the desired contrast quality, which inevitably leads to some adverse events. Herein, we develop a six-nuclei, apoptosis-targeting T_1 CA, Gd_6−ZnDPA nanoprobe, which consists of a hexanuclear gadolinium nanocluster (Gd_6) with an apoptosis-targeting group (ZnDPA). The amplification of Gd(III) by the hexanuclear structure generates its high longitudinal relaxivity (44.67 mM^{-1} s^{-1}, 1T) and low r_1/r_2 ratio (0.68, 1T). Based on the Solomon−Bloembergen−Morgan (SBM) theory, this notable improvement is primarily ascribed to a long correlation tumbling time (τ_R). More importantly, the Gd_6−ZnDPA nanoprobe shows excellent tumor apoptosis properties with an enhanced MR signal ratio (~74%) and a long MRI imaging acquisition time window (~48 h) in 4T1 tumor-bearing mice. This study introduces an experimental gadolinium-based CA for the potential imaging of tumor apoptosis in the context of MRI.

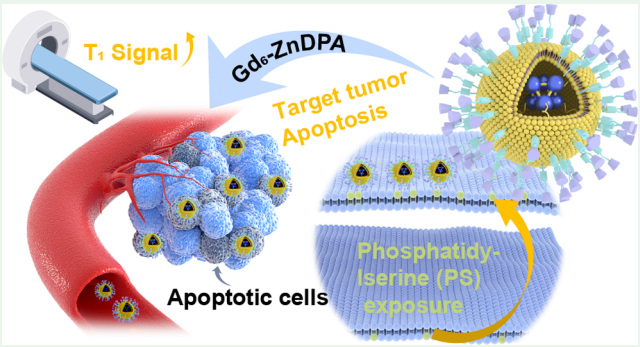

KEYWORDS: *magnetic resonance imaging (MRI), apoptosis, tumor, gadolinium, contrast agent, nanoprobes*

1. INTRODUCTION

Cancer continues to pose a significant threat to global health, with approximately 10 million fatalities annually.[1] The principal therapeutic approach, particularly in pre- and postoperative contexts, is chemotherapy, which effectively eradicates cancer cells through the induction of programmed cell death (PCD) or apoptosis.[2,3] Nevertheless, individual differences in response to chemotherapy require prompt evaluation of how tumors react to the treatment, allowing for the optimization of individualized antitumor regimens to enhance the treatment efficacy.[4] Apoptosis is characterized by plasma membrane asymmetry, culminating in the externalization of phosphatidylserine (PS) on the cell surface.[5] Annexin V is a protein that is predominantly utilized in cell biology for the identification of apoptotic cells due to its high affinity for PS. However, the inherent instability of Annexin V proteins presents a significant obstacle.[6] Currently, an anion recognition group, zinc(II)-dipicolylamine (ZnDPA), has been recognized for its selective binding to PS.[7,8] In addition, because it is both affordable and easy to obtain, ZnDPA emerges as a promising substitute for Annexin V in the development of probes specifically targeting apoptotic cells.

Magnetic resonance imaging (MRI) is a widely used noninvasive technique in clinical diagnosis, acclaimed for its elevated spatial resolution and remarkable contrast properties in body tissue visualization. In MRI, contrast agents (CAs) are crucial as they enhance image contrast by affecting the relaxation efficiency of water protons in the surrounding tissue. The most commonly used CAs for clinical purposes are gadolinium-based CAs (GBCAs).[9] Gadolinium (Gd III), a trivalent metal ion with seven unpaired electrons, is highly paramagnetic.[10] While free gadolinium is a toxic heavy metal, its complexes are employed in medical applications because of their low toxicity and ability to improve the longitudinal (T_1) relaxation rates (r_1) of surrounding protons and coordinate water molecules.[11,12] However, due to the low content of Gd(III) in traditional commercial GBGAs (Magnevist, Omniscan, Gadavist, etc.), a high dosage is typically

Received: January 24, 2024
Revised: March 21, 2024
Accepted: March 25, 2024
Published: April 4, 2024

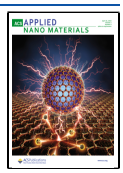

Scheme 1. Schematic Illustration of the Gd_6–ZnDPA Manufacturing Process and the Mechanism Underpinning their MR Imaging Capabilities with Apoptotic Tumor Cells

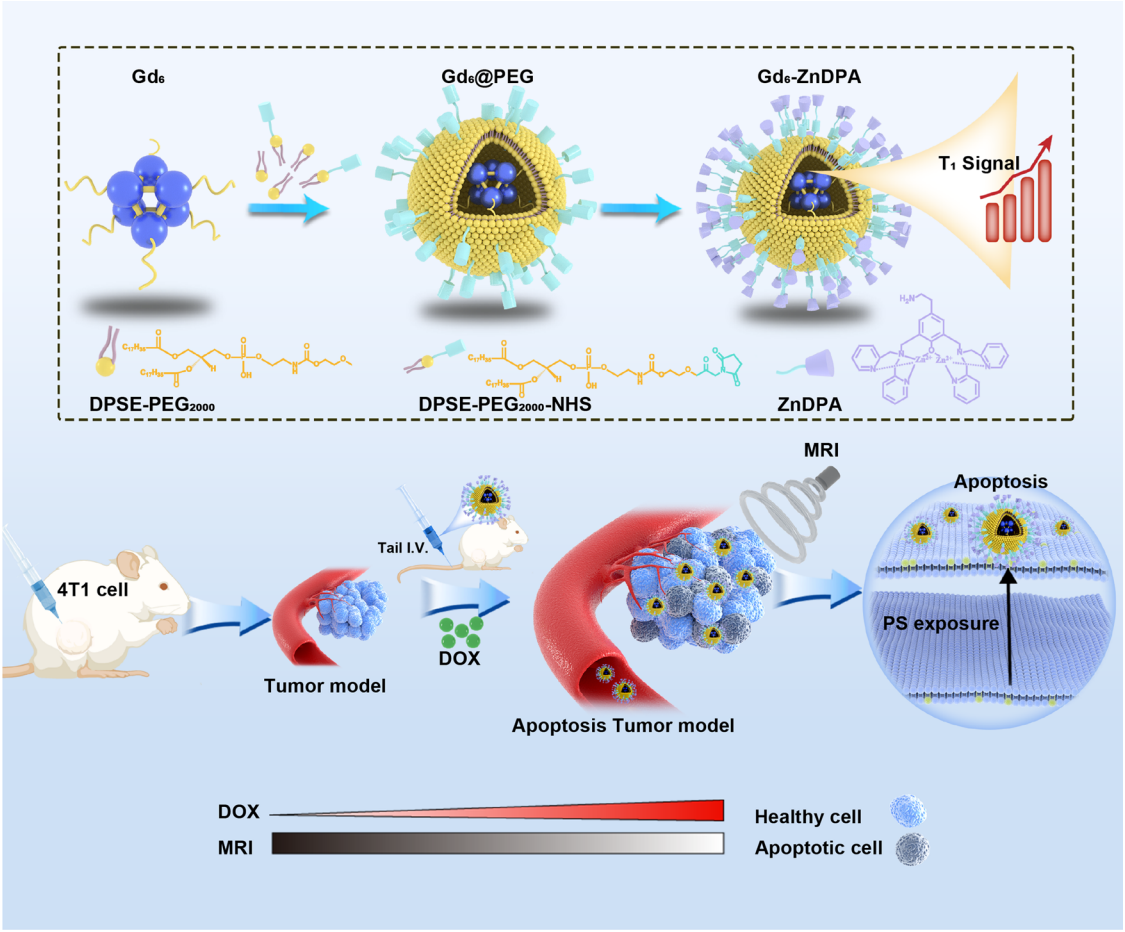

administered to patients.[13] This can potentially cause severe adverse reactions such as nephrotoxicity (e.g., nephrogenic systemic fibrosis), especially in patients with renal injury, as well as the deposition and retention of Gd(III) metal in human tissues.[14−16] Hence, it is critically important to advance the development of gadolinium-based contrast agents (GBCAs) that offer enhanced relaxivity and sensitivity alongside a reduction in the necessary injection dosage to mitigate potential adverse effects.

For example, Du et al.[17] and Lu et al.[18] reported enhanced r_1 values through the covalent incorporation of Gd-chelates into macromolecular complexes. However, a limitation of these macromolecules is their finite number of coupling sites, which restricts their payload capacity for metal ions.[19] Recently, researchers have been increasingly focusing on gadolinium-based nanoparticles (Gd-NPs). This interest is driven by the unique nanoscale geometric confinement of Gd-NPs, which sets them apart from conventional chemical agents. Examples include Gd_2O_3,[20,21] Gd_{140},[22] and Gd-IR780[23] nanoprobes, each characterized by a larger surface-area-to-volume ratio and functionalization properties.[24] These nanoparticles effectively address the payload limitation, achieving a higher r_1 value and enabling the conjugation of multiple functional molecules, thereby improving targeting capabilities.

Herein, we introduce a hexanuclear Gd(III) cluster (Gd_6) conjugated with ZnDPA, forming the tumor apoptosis-targeting T_1 CAs known as Gd_6–ZnDPA nanoparticles (Gd_6–ZnDPA NPs). On the one hand, one hexanuclear polyhedron loaded with six Gd(III) ions exhibits favorable r_1 values. On the other hand, by linking Gd_6 nanoclusters with ZnDPA ligands, which demonstrate a strong affinity with PS, we transition from traditional passive targeting to an active targeting strategy. This approach significantly enhanced the site-specific localization efficiency while minimizing non-specific biodistribution.[25] Therefore, Gd_6–ZnDPA NPs have been utilized as MRI CAs to precisely monitor the apoptosis of 4T1 tumors in response to chemotherapy, even at low intravenous levels (Scheme 1).

2. EXPERIMENTAL SECTIONS

2.1. Material and Reagents. Fluorene, carbon disulfide, 2-chloro-2-methylpropane, dichloromethane, *N*-bromosuccinimide, 1,3-dimethylpropionic acid (^{t}BuCO$_2$H), and gadolinium(III) oxide (Gd_2O_3) were purchased from Adamas-β Co. Ltd. Hydrochloric acid, petroleum ether, tetrahydrofuran, methyl alcohol, and methyl alcohol were purchased from General Reagent Inc. 2-Distearoyl-*sn*-glycero-3-phosphoethanolamine (DSPE)–poly(ethylene glycol)$_{2000}$ (PEG_{2000}), DSPE–PEG_{2000}–*N*-hydroxy succinimide (NHS), and ZnDPA were purchased from Xi'an Ruixi Biotech Inc. DSPE–PEG_{2000}–fluorescein isothiocyanate (FITC) was purchased from Ponsure Biotech Inc. Mouse breast cancer cells (4T1) were obtained from the Shanghai Institutes of Biological Sciences. The Cell Counting Kit-8 (C0037) was purchased from Beyotime (Jiangsu, China). Balb/c mice were purchased from Jiesijie Laboratory Animal Co. Ltd.

https://doi.org/10.1021/acsanm.4c00511
ACS Appl. Nano Mater. 2024, 7, 9020−9030

2.2. Synthesis Processes. *2.2.1. Synthesis of $Gd_6(OH)_2(FluPO_3)_3(^tBuCO_2)_{10}(H_2O)_6$.* 2,7-Di-*tert*-butyl-9-methyl-9*H*-fluoren-9-yl phosphonic acid ($FluPO_3$) was synthesized according to a previous report.[26] Gd_2O_3 (3.625 g, 10 mmol) and 1,3-dimethylpropionic acid ($^tBuCO_2H$) (50 g, 500 mmol) were added to a three-neck flask and heated to 160 °C for 24 h. After the mixture was cooled to room temperature, 100 mL of toluene was added and heated to 110 °C for 2 h, followed by filtering and evaporation to produce $Gd_2(^tBuCO_2)_6(^tBuCO_2H)_6$. $FluPO_3H$ (0.0374 g, 0.1 mmol), $Gd_2(^tBuCO_2)_6(^tBuCO_2H)_6$ (0.1532 g, 0.1 mmol), and $^tBuCO_2H$ (0.0408 g, 0.4 mmol) were added to a mixture of acetonitrile (8 mL) and dichloromethane (8 mL) and then stirred for 24 h; the colorless rhombus-shaped crystal $Gd_6(OH)_2(FluPO_3)_3(^tBuCO_2)_{10}(H_2O)_6$ was obtained after filtering and evaporation.

2.2.2. Synthesis of Gd_6@PEG NPs. 5 mg of Gd_6 was dissolved in chloroform (10 mL) by sonicating, and then DSPE−PEG_{2000} (10 mg) was added. Then, sonication and shaking were continued for 10 min. The well-mixed solvents were added with 10 mL of ddH_2O, followed by another 10 min of sonication and shaking before rotary evaporation and filtration; the aqueous solution of DSPE−PEG_{2000} coated with Gd_6 nanoparticles obtained was referred to as Gd_6@PEG.

2.2.3. Synthesis of Gd_6−ZnDPA NPs. Five milligrams of Gd_6 were dissolved in chloroform (10 mL) by sonication; then, DSPE−PEG_{2000} and DSPE−PEG_{2000}−NHS (8 and 2 mg, respectively) were added and subjected to sonication and shaking for 10 min. The well-mixed solvents were added with 10 mL of ddH_2O, followed by another 10 min of sonication and shaking before rotary evaporation and filtration; then, the solution was added with 3 mg of ZnDPA and stirred (37 °C, 12 h); after repeating the filtration, evaporation, and centrifugation (ultrafiltration tube, 10 kDa, 3500 rpm, 8 min), the Gd_6−ZnDPA NP solution was collected under an atmosphere of flowing dry nitrogen.

2.2.4. Synthesis of Gd_6−ZnDPA/FITC NPs. Five milligrams of Gd_6 were dissolved in chloroform (10 mL) by sonicating; then, DSPE−PEG_{2000} (6 mg), DSPE−PEG_{2000}−NHS (2 mg), and DSPE−PEG_{2000}−FITC (2 mg) were added and subjected to sonication and shaking for 10 min. The well-mixed solvents were added with 10 mL of ddH_2O, followed by another 10 min of sonication and shaking before rotary evaporation and filtration; then, the solution was added with 3 mg of ZnDPA and stirred (37 °C, 12 h); after repeating the filtration, evaporation, and centrifugation (ultrafiltration tube, 10 kDa, 3500 rpm, 8 min), Gd_6−ZnDPA NP solutions were collected under an atmosphere of flowing dry nitrogen.

2.3. X-ray Crystallography Analysis. The diffraction intensity for the Gd_6 cluster was measured using the hemisphere technique on a Bruker SMART Platform CCD diffractometer at 298 K, with a molybdenum tube ($\lambda\kappa\alpha$ = 0.71073 Å). The absorption correction was implemented using SADABS program. The structure was then resolved and refined through a full-matrix least-squares approach based on F^2. This was carried out using the SHELXS-97 and SHELXL-97 program packages, respectively. During refinement, all of the nonhydrogen atoms were treated anisotropically. The calculations involved using analytical expressions for the scattering factors of neutral atoms and corrections for anomalous dispersion were also incorporated into the analysis.

2.4. X-ray Photoelectron Spectroscopy (XPS) Analysis. Chemical elements and bonds of the samples were analyzed by X-ray photoelectron spectroscopy (XPS, Thermo Scientific Escalab 250Xi). Each analysis started with a survey from 0 to 800 eV. The C 1s photoelectron line at 284.79 eV was used for the calibration of spectra. The O 1s, C 1s, P 2p, and Gd 4d lines were recorded for each specimen.

2.5. Measurement of the Longitude Relaxivity of Gd_6@PEG NPs. The readymade Gd_6@PEG NPs and Gd-DTPA (MAGNEVIST) were dispersed into deionized water with a microcentrifuge tube (1.5 mL), separately. Then, T_1-weighted images with different [Gd] concentrations (0, 0.0125, 0.025, 0.0375, 0.05, 0.075, and 0.1 mM) were observed using the 1T magnetic resonance imaging apparatus, respectively. Meanwhile, both the longitudinal relaxivity rate ($r_1 = 1/T_1$) and transverse relaxivity ($r_2 = 1/T_2$) of Gd_6@PEG NPs and Gd-DTPA under different [Gd] concentrations were calculated, respectively. The measurement parameters were set as follows: repetition time (TR) = 545 ms; echo time (TE) = 10 ms; field-of-view (FOV) = 45 mm; slice thickness = 3 mm; average = 2.

2.6. Nuclear Magnetic Relaxation Dispersion (NMRD) Measurements. Gd-DTPA and Gd_6@PEG NP solutions at a [Gd] concentration of 0.1 mM were placed in a field-cycling relaxometer (SMARtracer, Stelar), respectively. The $1/T_1$ NMRD profiles of solvent protons were measured over the magnetic field range of 0.00025−3T (corresponding to about 10^4 to 1.27×10^8 Hz proton Larmor frequency). The longitudinal relaxation time was obtained from the instruments directly in the range of 0.0025−0.5 T, while the longitudinal relaxation time in 3T was fitting by formula (1). The nuclear magnetic relaxation dispersion profiles of MRI contrast agents were analyzed based on the Solomon−Bloembergen−Morgan (SBM) theory using Matlab software.

$$\mathrm{STI} = S*(1 - 2*e^{-T_I/T_1}) \quad (1)$$

where STI is the signal intensity at a given inversion time (T_I), S is the maximum signal intensity that can be achieved if there are no relaxation effects, e denotes the base of the natural logarithm, T_I is the inversion time, and T_1 is the longitudinal relaxation time.[27]

2.7. Biocompatibility and Cytotoxicity of Gd_6@PEG and Gd_6−ZnDPA NPs. A hemolysis test was carried out to analyze the blood compatibility of the Gd_6@PEG and Gd_6−ZnPA NPs in vitro. All of the steps refer to GB/T 14233.1−2022. A 2% (v/v) erythrocyte suspension was used in the assay. 2 mL of fresh whole blood of two Balb/c mice (about 5 weeks old, 25−30 g) were centrifuged at 1500 rpm for 5 min. The obtained erythrocyte suspension was rinsed with phosphate-buffered saline (PBS) three times, followed by further dilution to a final concentration of 2% (v/v) erythrocyte suspension. Next, five centrifugal tubes containing 500 μL of 2% (v/v) erythrocyte suspension were prepared and then added with 500 μL of Gd_6@PEG or Gd_6−ZnPA NPs solutions with different concentrations (12.5, 25, 50, 100, and 200 μg mL^{-1}) as two experimental groups, while 500 μL of PBS and 500 μL of ddH_2O were considering as the negative and positive groups, respectively. After incubation at 37 °C for 2 h, these samples were centrifuged at 1000 rpm for 3 min, the upper supernatant was then taken into a 96-well plate, and the absorbance (A) at 545 nm was measured; each group was repeated 3 times, and the average value was taken to calculate the hemolysis rate.

The mouse breast cancer cells (4T1) were plated at a density of 6000 cells/well in 96-well plates and incubated with 100 μL of completed medium (high glucose Dulbecco's modified Eagle's medium added with 10% fetal bovine serum and 1% penicillin/streptomycin) for 2 h, at 37 °C and 5%CO_2. When cells were attached, new medium containing different concentrations (0, 12.5, 25, 50, and 100 μg mL^{-1}, which were regarded as control and experimental groups) of Gd_6@PEG or Gd_6−ZnPA NPs was replaced every 6 and 12 h separately, followed by the addition of CCK-8 reagent. After incubating the mixed solutions, the absorbance values (A) of each group were detected at 450 nm using a microplate reader (SPR-960, Sunostik Medical Technology Co. Ltd.). The cell viability was counted through the following equation.

$$\text{cell viability (\%)} = A_{\text{experiment}}/A_{\text{control}} \times 100\% \quad (2)$$

2.8. Confocal Laser Scanning Microscopy (CLSM) Imaging for Apoptotic Cells In Vitro. 4T1 cells were separated into three experimental groups: apoptotic 4T1 cells (apoptosis group), apoptotic 4T1 cells treated with Gd_6−ZnPA/FITC (targeting group), and apoptotic 4T1 cells treated with ZnDPA (50 μg mL^{-1}, 1 h) before Gd_6−ZnDPA/FITC treatment (blocking group). 4T1 cells of all three groups were incubated with Gd_6−ZnDPA (50 μg mL^{-1}) for 2 h at 37 °C with 5% CO_2. Then, the cells were rinsed with PBS, and fresh media was added for confocal laser scanning microscopy (CLSM).

2.9. T_1-Weighted MRI Imaging Performance In Vivo. The apoptotic tumor model mice were used to evaluate the apoptosis-targeting performance of Gd_6−ZnPA NPs. These mice were inoculated subcutaneously with approximately 5×10^6 4T1 cells into the front flank, obtaining the ideal tumor sizes of 100−200 mm^2

https://doi.org/10.1021/acsanm.4c00511
ACS Appl. Nano Mater. 2024, 7, 9020−9030

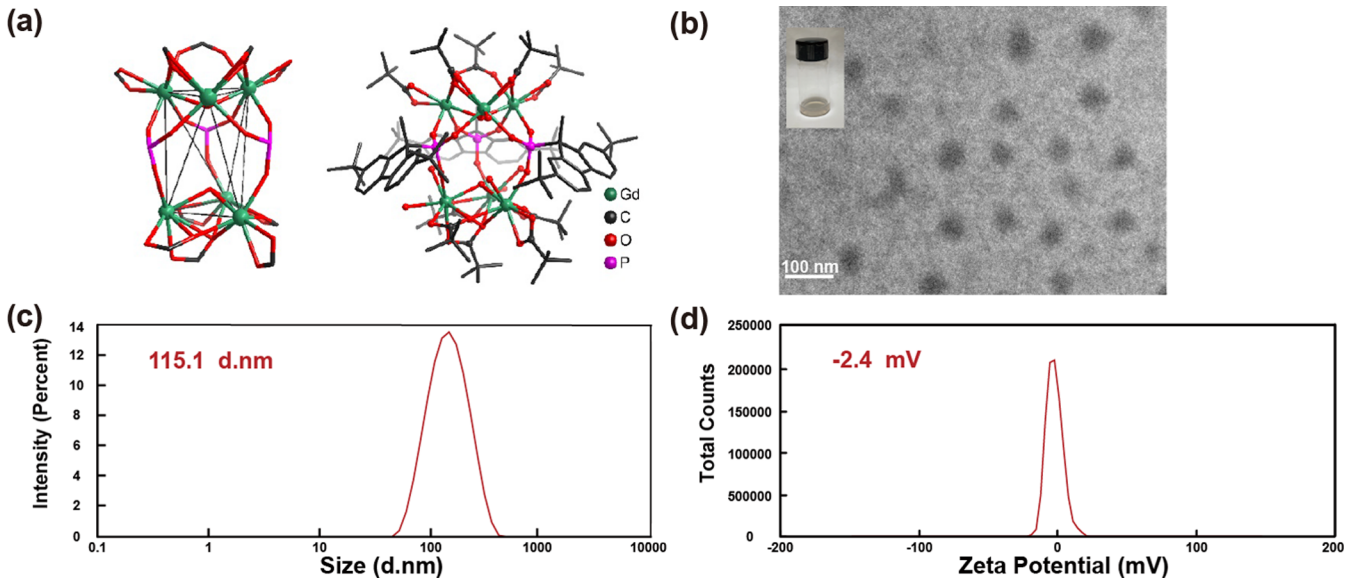

Figure 1. (a) Single-crystal X-ray structure of Gd_6. (b) Transmission electron microscopy (TEM) images (scale bar: 100 nm) of Gd_6@PEG. (c) Size distribution and (d) ζ-potential distribution of Gd_6@PEG NPs.

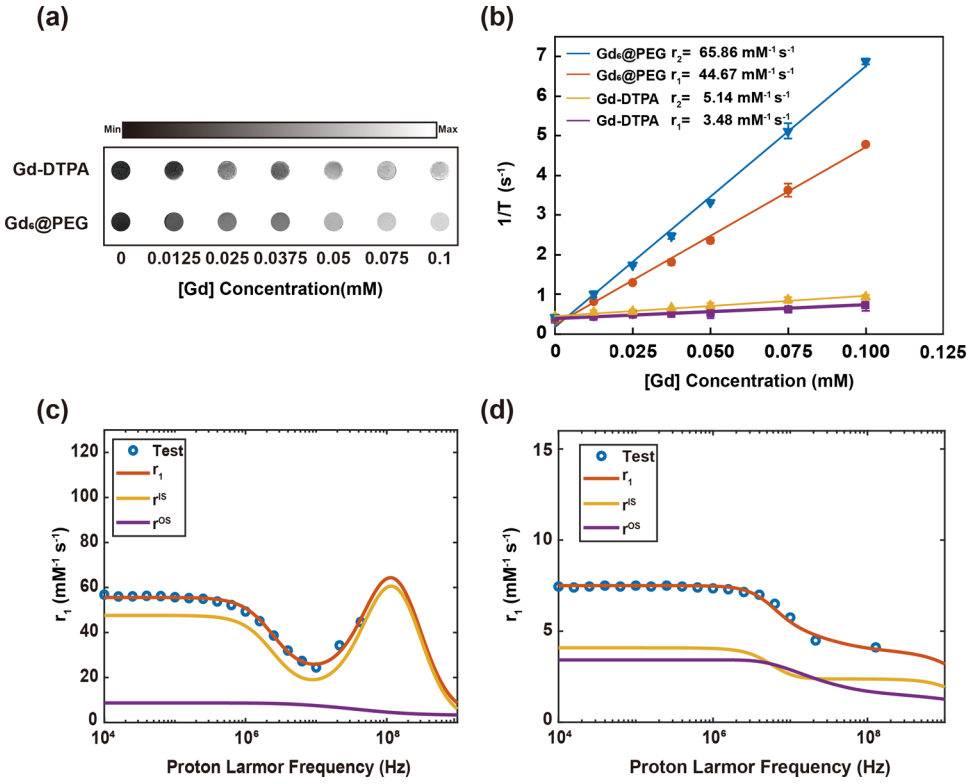

Figure 2. (a) In vitro T_1-weighted images, (b) longitudinal relaxation rates (r_1), and transverse relaxation rates (r_2) of Gd_6@PEG and Gd-DTPA with different [Gd] concentrations of 0, 0.0125, 0.025, 0.05, 0.075, and 0.1 mM at the 1T system. Longitudinal relaxivity (r_1) distributions of (c) Gd_6@PEG and (d) Gd-DTPA under different hydrogen proton Larmor frequencies [1×10^4 to 1.27×10^8 Hz (0.00025−3T)] and fitting curves based on the Solomon−Bloembergen−Morgan (SBM) paramagnetic relaxation theory.

after 7−10 days, to develop 4T1 tumor model mice. Then, they were injected with 10 mg kg^{-1} doxorubicin hydrochloride (DOX·HCl) every 3 days for a total of two times in order to establish the apoptotic tumor model.[7] The targeting group (i.v. Gd_6−ZnPA solutions at a level of 0.0025 mmol kg^{-1}) and the blocking group (i.v. ZnDPA at a level of 0.008 mmol kg^{-1} for 15 min before injecting the same dosage of Gd_6−ZnPA solutions) were further assessed for the contrast-forming properties of Gd_6−ZnPA NPs in vivo. In addition, mice bearing only the 4T1 tumor were administrated with Gd-DTPA or Gd_6−ZnPA at a level of 0.0025 mmol kg^{-1}; then T_1-weighted images of each group were obtained at different time points (0, 1.5, 5, 9, 24, and 48 h) with a 3.0T MRI system. The measurement parameters were set as follows: repetition time (TR) = 1371 ms; echo time (TE) = 13.62 ms; field-of-view (FOV) = 35 mm; slice thickness = 1 mm; average = 6.

In addition, the relative signal enhancement (RSE %) in the tumor, heart, bladder, kidney, and liver was calculated to qualify MR signal intensity changes. The equation is as follows:

https://doi.org/10.1021/acsanm.4c00511
ACS Appl. Nano Mater. 2024, 7, 9020−9030

$$\text{RSE}\ \% = (\text{SI}_{\text{post}}/\text{SI}_{\text{muscle}'} - \text{SI}_{\text{pre}}/\text{SI}_{\text{muscle}})/\text{SI}_{\text{pre}}/\text{SI}_{\text{muscle}} \times 100\% \quad (3)$$

where SI indicates the signal intensity of the region of interest (ROI),[28] SI_{pre} SI_{post}, $\text{SI}_{\text{muscle}}$, and $\text{SI}_{\text{muscle}'}$ represent the signal intensities of the corresponding areas before and after injection into the tail vein of mice, respectively.

2.10. Distribution and Metabolism of Gd_6–ZnDPA NPs. Female Balb/c mice (about 5 weeks old, 25–30 g) were injected intravenously with Gd_6–ZnDPA NPs at a dose of 0.0025 mmol kg^{-1}. As the nanoparticles flow into the body along with the bloodstream, coronal scanning images were acquired via a 3.0T MRI system (uMR790, United imaging) to determine the accumulation and metabolism of nanoparticles in specific organs, including the liver, kidney, and bladder, at 0, 30, 60, 90, 120, 150, and 180 min, respectively. All animals involved in the experiments were treated according to the Guidelines for Care and Use of Laboratory Animals and protocols approved by the Shanghai Normal University.

2.11. Statistical Analysis. Data were expressed as mean ± standard deviation. Statistical analysis was conducted by one-way analysis of variance (ANOVA) with Tukey's significant difference post hoc test using GraphPad Prism 9.0 (GraphPad Software, Inc.). *P < 0.05, ** P < 0.01, and *** P < 0.001.

3. RESULTS AND DISCUSSION

3.1. Characterization of $Gd_6(OH)_2(FluPO_3)_3(^tBuCO_2)$-$10(H_2O)_6$. Figure 1a displays the single-crystal X-ray diffraction pattern of the Gd_6 cluster, revealing that Gd_6 is a neutral hexanuclear complex that crystallized in the monoclinic space group C_2, which contains six Gd(III) ions, three phosphonate ligands, 10 pivalates, two μ_3-OH groups, and six water molecules. The six Gd(III) can be divided into two trinuclear metal units, which can be viewed as a μ_3-OH-bridged trimer. The trimers are connected by three μ_3-η^1:η^1:η^1-PO_3 groups of three phosphonate ligands, forming a trigonal antiprism structure with a similar configuration. The specific crystallographic parameters of the Gd_6 cluster are presented in Table S1. In addition, the steric hindrance effect of this trigonal antiprism Gd_6 cluster is particularly strong because each of its trigonal surfaces is wrapped by five tertiary butyl groups from five pivalates, while its side faces are surrounded by three large aromatic groups from three phosphonate ligands. The coordination-driven self-assembly method between metal ions and organic linkers has been a promising strategy for developing polynuclear Ln-assemblies.[29,30] The XPS survey spectra of Gd_6 are shown in Figure S2a. The peaks at 141.9,

Table 1. Parameters of Gd_6@PEG and Gd-DTPA Based on the SBM Theory

contrast	Gd_6@PEG	Gd-DTPA
q	1	1
τ_R (ps)	600	77
τ_m (ns)	12	142

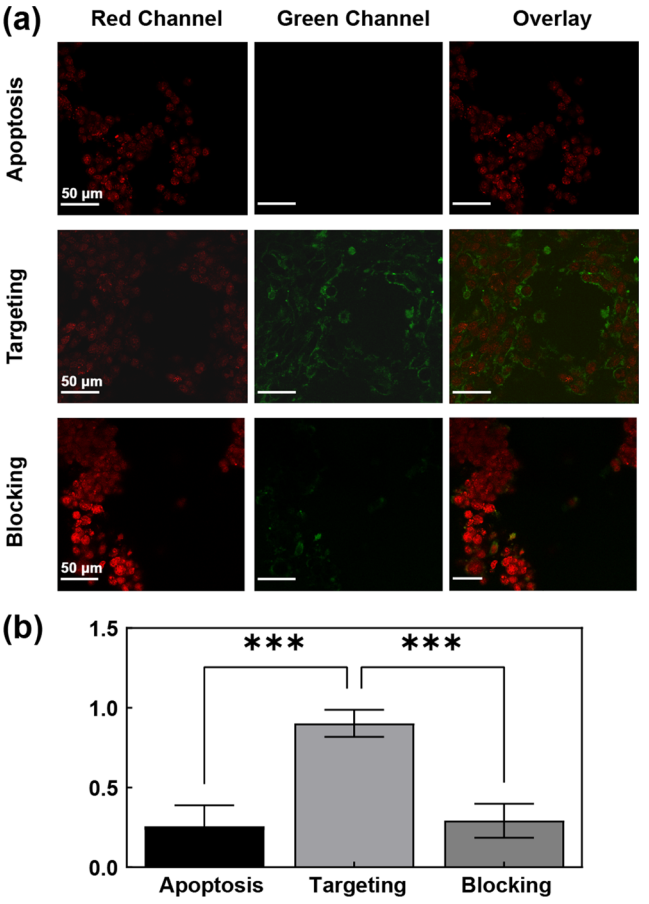

Figure 4. (a) Confocal laser scanning microscopy (CLSM) images of apoptotic 4T1 cells incubated with Gd_6–ZnDPA/FITC for 2 h at 37 °C (from left to right: different channels of apoptotic 4T1 cells; red channel: collected from 575 to 595 nm; green channel: collected from 515 to 535 nm; overlay: field between green and red channels). 4T1 cells were incubated with DOX (5 μg mL^{-1}) for 4 h to obtain the "apoptotic group", Then, apoptotic cells were incubated with Gd_6–ZnDPA/FITC (50 μg mL^{-1}) for another 2 h to derive the "targeting group" or they were incubated by ZnDPA (50 μg mL^{-1}) for 1 h before incubating with Gd_6–ZnDPA/FITC (50 μg mL^{-1}) to obtain the "blocking group". (b) Fluorescence intensity ratio of the green channel to the red channel. ***P < 0.001 versus any other group.

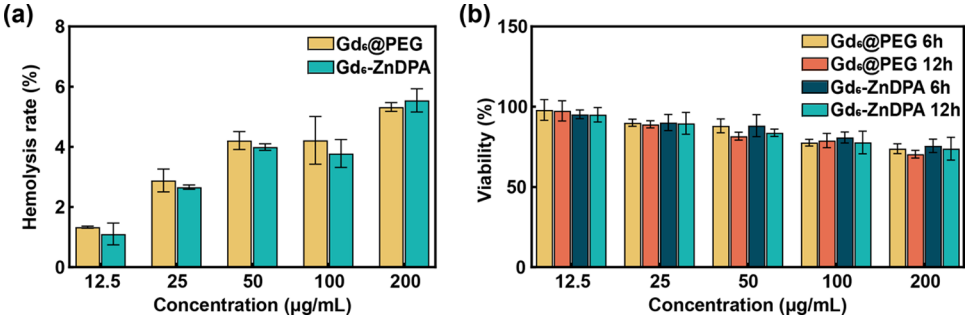

Figure 3. (a) Hemolysis rate assessment of Gd_6@PEG and Gd_6–ZnDPA NPs with different [Gd] concentrations. (b) Relative cell viabilities of 4T1 cells after coincubation with Gd_6@PEG and Gd_6–ZnDPA NPs at 6h and 12 h (n = 3).

https://doi.org/10.1021/acsanm.4c00511
ACS Appl. Nano Mater. 2024, 7, 9020–9030

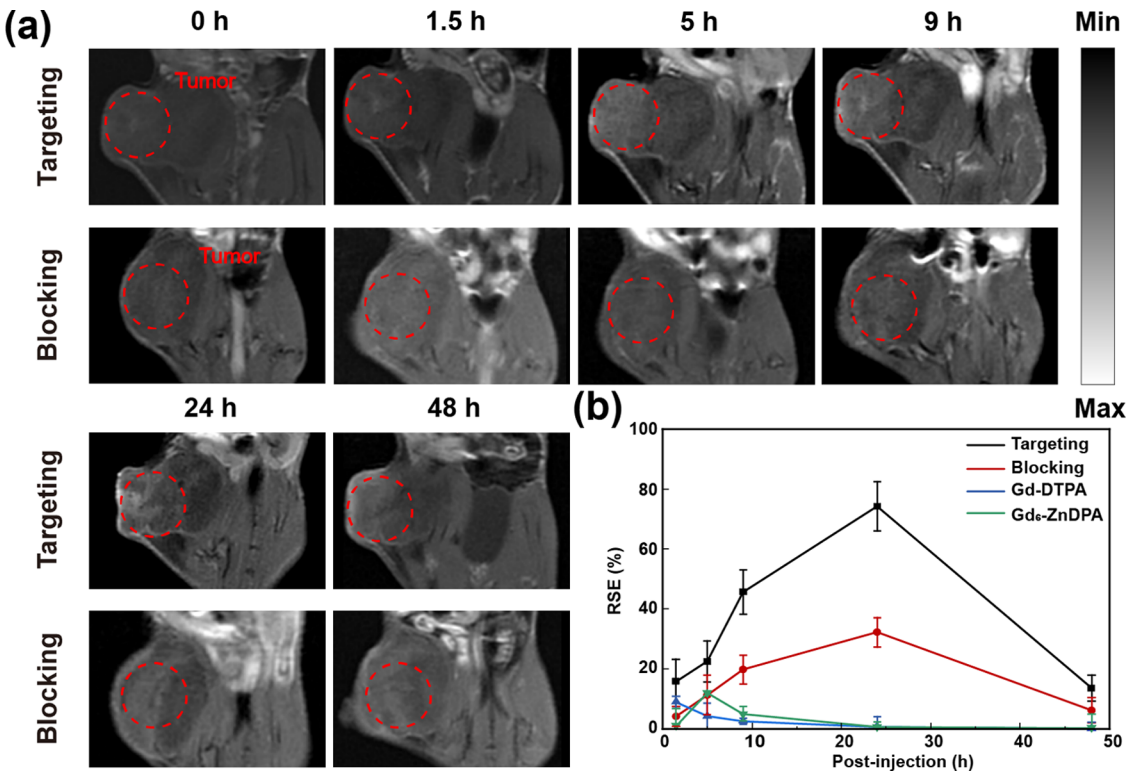

Figure 5. (a) In vivo T_1-weighted images of apoptotic 4T1 tumor model mice after intravenous administration of Gd_6−ZnDPA NPs (0.0025 mmol kg^{-1}) at 3T. (b) Relative signal enhanced (RSE) ratio at the tumor site at 1.5, 5, 9, 24, and 48 h post-injection.

143.1, 284.8, and 530.8 eV correspond to the P 2p, Gd 4d, C 1s, and O 1s peaks, respectively. Figure S2b clearly shows the peak of C═C (284.16 eV), C−C (288.43 eV), and O═C−O (284.92 eV);[31] the peak area of C−C is very small compared with other peaks, reflecting the low content of C−C. As shown in Figure S2c, O 1s was fitted into four peaks of 529.79, 531.15, and 532.24 eV, respectively, corresponding to Gd−O, C−O, and adsorbed H_2O.[31−33] The peaks of Gd 4d centered at 142.95 and 148.39 eV in Figure S2d are attributed to a pair of $4d_{5/2}$ and $4d_{3/2}$ doublets, which correspond to Gd−O.[34] The presence of Gd−O bonds clearly confirmed the formation of a Gd-based cluster. The P 2p peaks can be deconvoluted into two peaks, as shown in Figure S2e: 132.41 eV ($2p_{3/2}$ P−O) and 133.38 eV ($2p_{2/1}$ P−O).[35] The result of P peak splitting demonstrated the content of P−O bonds in the cluster. These observations agree with the single-crystal X-ray structure of Gd_6, as shown in Figure 1a. Thermogravimetric analysis (TGA) demonstrated the good thermal stability of Gd_6, the relative weight of which remains above 80% at temperatures between 0 and 300 °C (Figure S1a). Powder X-ray diffraction patterns of the as-synthesized Gd_6 showed good agreement with the data simulated from the single-crystal structure, indicating the purity of the bulk sample (Figure S1b). Gd_6 was encapsulated using 2-distearoyl-*sn*-glycero-3-phosphoethanolamine−poly(ethylene glycol) (DSPE−PEG_{2000}) in a 1:2 ratio to produce the water-soluble nanoparticles, Gd_6@PEG NPs. As shown in Figure 1b, transmission electron microscopy (TEM) analysis demonstrated that monodispersed Gd_6@PEG NPs were uniformly distributed. Additionally, TEM element mapping and energy-dispersive X-ray spectroscopy (EDX) spectra of Gd_6@PEG displayed in Figure S3 show that Gd_6 was encased with DSPE−PEG_{2000} successfully to form Gd_6@PEG, and elements C, O, P, S, and Gd were uniformly distributed in the NPs. Hydrodynamic diameters and ζ-potentials of Gd_6@PEG were 115.1 nm and −2.4 mV, respectively (Figure 1c,d). In summary, the rigid configuration and moderate size of Gd_6@PEG provide the advantage for the following application.

3.2. MRI Contrast Enhancement of Gd_6. T_1-weighted images obtained at a 1T magnetic field of both Gd_6@PEG and Gd-DTPA showed that Gd_6@PEG is more effective for biodiagnosis than Gd-DTPA as the concentration of [Gd] increases (Figure 2a). R_1 typically reflects the contrast efficiency of CAs, with a high r_1 value indicating superior contrast performance.[36] The longitudinal relaxivity (r_1) and transverse relaxivity (r_2) of Gd_6@PEG and Gd-DTPA in an aqueous solution were measured under a 1T MRI apparatus, respectively. The linear graph illustrated that not only did the relaxation rate related to the concentration of [Gd] linearly fit well, but the r_1 and r_2 values of Gd_6@PEG were relatively higher than those of Gd-DTPA, specifically ∼44.67 and ∼65.86 mM^{-1} s^{-1} versus ∼3.48 and ∼5.14 (Figure 2b). Furthermore, Gd_6@PEG appears to be a promising alternative to T_1-weighted MRI contrast agents, with a relaxation value of $r_2/r_1 \approx 1.47$ (<2).[37]

According to the Solomon−Bloembergen−Morgan (SBM) theory, the interaction between water protons and paramagnetic ions determines the relaxivity of GBCAs, which are classified into three mechanisms, including the inner sphere (r^{IS}), which means the magnetic center directly coordinates with water protons, the second sphere (r^{SS}), which means that water protons coordinate with the paramagnetic center through hydrogen bonds, and the outer sphere (r^{OS}), which describes molecules that require relaxation improvement without direct coordination.[24] In general, the T_1 relaxivity of a contrast agent is positively correlated with the tumbling time

https://doi.org/10.1021/acsanm.4c00511
ACS Appl. Nano Mater. 2024, 7, 9020−9030

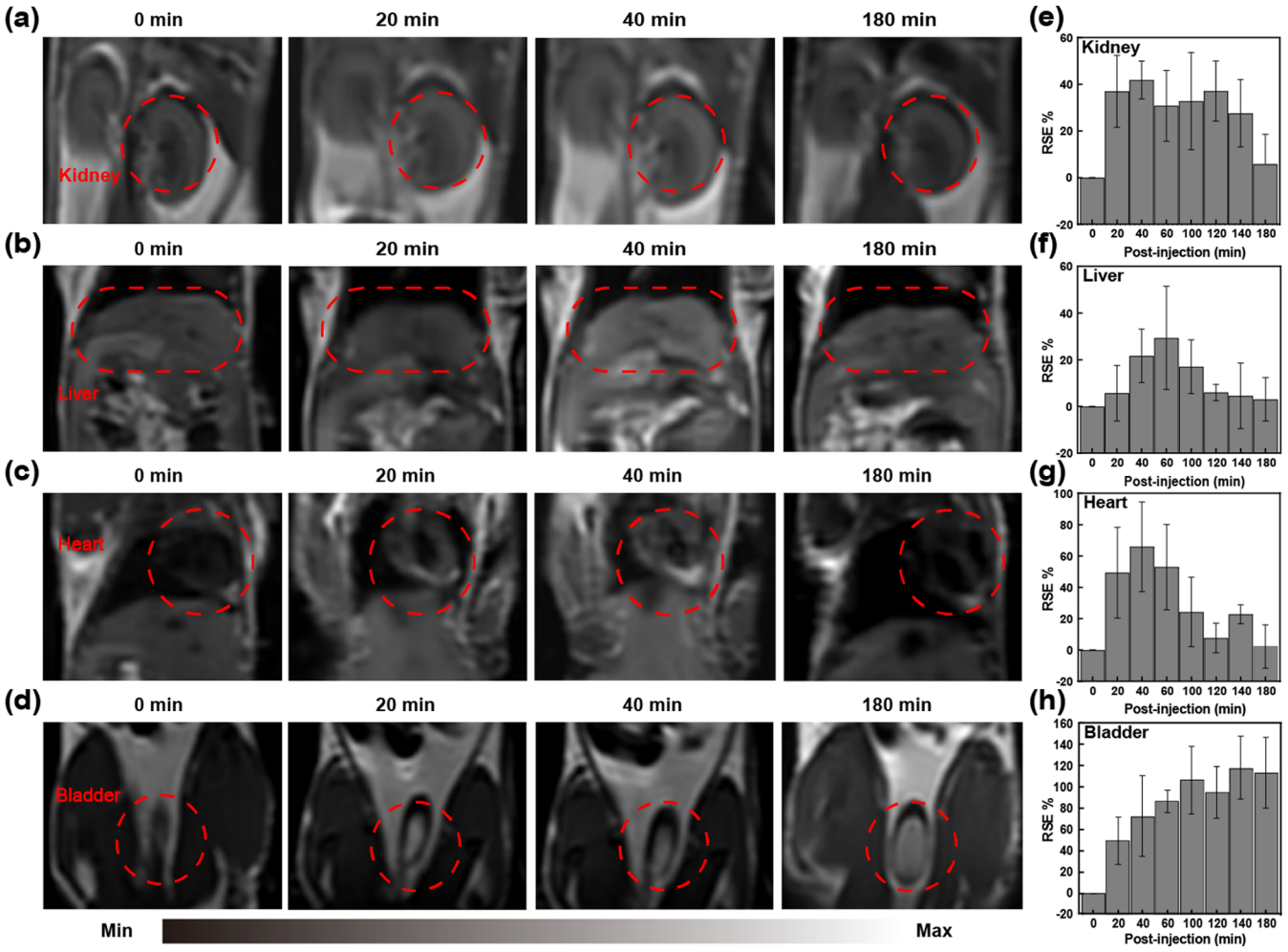

Figure 6. T_1-weighted MR images of the (a) kidney, (b) liver, (c) heart, and (d) bladder of Balb/c mice before and after intravenous injection of Gd_6–ZnDPA NPs (0.0025 mmol kg^{-1}) at 3T. The relative signal enhanced ratio (RSE %) in the (e) kidney, (f) liver, (g) heart, and (h) bladder were recorded at specific time points throughout 180 min post-injection.

of the molecule (τ_R), the proton residence lifetime ($1/\tau_m$), and the coordinating number of the proton (q).[38] To further investigate the properties of Gd_6@PEG, we measured the longitudinal relaxivity (r_1) values of Gd_6@PEG and Gd-DTPA at different field strengths [$1/T_1$ nuclear magnetic relaxation dispersion (NMRD) profiles] and compared the relative physical–chemical parameters based on the SBM theory. The NMRD profiles indicated that the r_1 value of Gd_6@PEG was consistently significantly higher than that of Gd-DTPA within a Larmor frequency of approximately 1×10^4 to 1.27×10^8 Hz, i.e., within 0.00025 to 3T. When the proton Larmor frequency ranges from 2.13×10^7 to 1.27×10^8 Hz (0.5–3T), the r_1 value of Gd_6@PEG NPs, which was predominated by the inner sphere, boosts drastically and peaks at 1.27×10^8 Hz (3T) (Figure 2c). In contrast, the r_1 value of Gd-DTPA continuously declines as the contribution of both the inner sphere and the outer sphere gradually decreases (Figure 2d). As is shown in Table 1, the τ_R of Gd_6@PEG (600 ps) is nearly 8-fold that of Gd-DTPA (77 ps), which may be attributed to its high molecular weight (3227.5 Da) and rigid hexanuclear crystalline structure, both of which can effectively decrease the tumbling time of the water protons.[19] Meanwhile, in terms of the proton residence lifetime (τ_m), Gd_6@PEG showed significantly lower data (τ_m = 12 ns) compared with Gd-DTPA(τ_m = 142 ns), which means a higher water exchange rate in Gd_6@PEG.[39] In conclusion, it is the synergistic functioning of these positive features that achieved the desirable T_1 relaxivity of Gd_6@PEG.

3.3. Targeting Property of Gd_6–ZnDPA NPs In Vitro.

Our preliminary study demonstrated the viability of Gd_6@PEG NPs as the T_1 CAs. Further exploration of the apoptosis-targeting potential of NPs is required. Because ZnDPA binds powerfully to turnover proteins (phosphatidylserine, PS) on the surface of apoptotic cells,[8] Gd_6 was first encased in DSPE–PEG_{2000} and DSPE–PEG_{2000}–*N*-hydroxy succinimide (NHS) to develop water-soluble Gd_6@PEG. Next, Gd_6@PEG was coupled with ZnDPA to develop Gd_6–ZnDPA NPs, which were capable of targeting apoptotic cells. The ζ-potentials and hydrodynamic diameters of Gd_6–ZnDPA NPs are given in Figure S4a,c. The ζ-potential increased from −2.4 to 11.8 mV, reflecting the positive property of ZnDPA. The hydrodynamic diameter of the nanoparticle changed slightly, from 115.1 to 132.6 nm, further confirming the combination. The TEM image demonstrated the spherical shape of Gd_6–ZnDPA NPs (Figure S4b). Additionally, the longitudinal relaxivity (r_1) of Gd_6–ZnDPA NPs in an aqueous solution was also measured using a 1T MRI apparatus. Although the r_1 value of Gd_6–ZnDPA (21.30 mM^{-1} s^{-1}) was decreased compared to that of Gd_6@PEG (44.67 mM^{-1} s^{-1}), it was still desirable (Figure S5). Inductively coupled plasma-atomic emission spectrometry

https://doi.org/10.1021/acsanm.4c00511
ACS Appl. Nano Mater. 2024, 7, 9020–9030

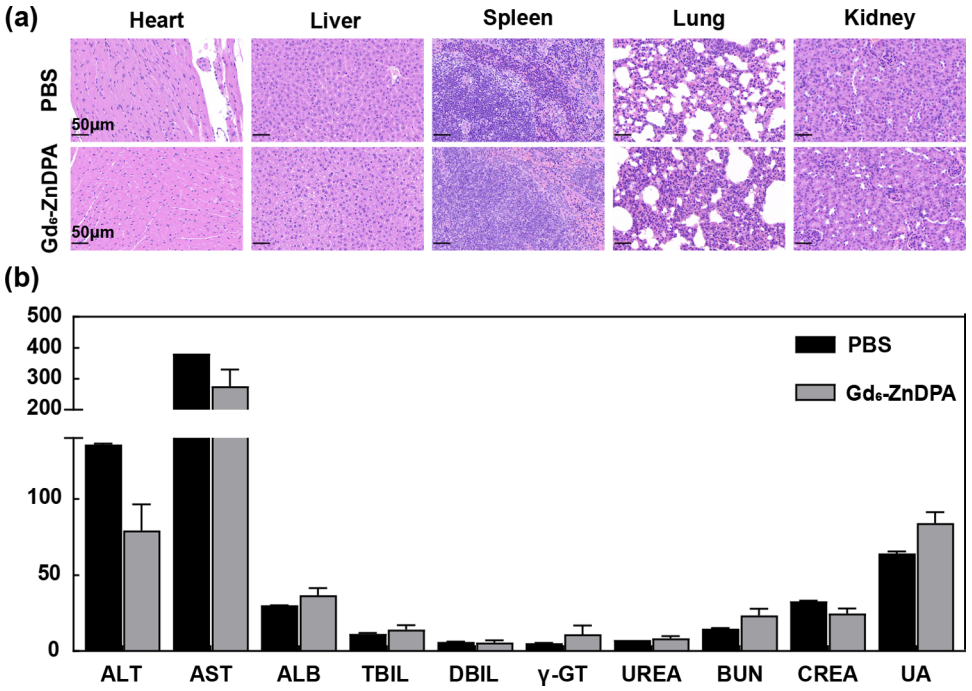

Figure 7. (a) H&E staining of the heart, liver, spleen, lung, and kidney of mice after intravenous administration with PBS × 1 and Gd_6−ZnDPA NPs (0.0025 mmol kg^{-1}); scale bar = 50 μm. (b) Results of serum biochemical indicators in mice, including ALT (U L^{-1}), AST (U L^{-1}), ALB (g L^{-1}), TBIL (μmol L^{-1}), DBIL (μmol L^{-1}), γ-GT (U L^{-1}), UREA (mmol L^{-1}), CREA (μmol L^{-1}), BUN (mmol L^{-1}), and UA (μmol L^{-1}) (n = 3).

(ICP-AES) showed that the Zn(II) element increased substantially to 0.69% while the percentage of Gd(III) elements decreased by approximately half, and the Gd_6 cluster accounts for 9.17% of the total molecules (Table S2).

In terms of in vivo imaging, the biocompatibility and safety of the nanoparticles are crucial. The hemolysis rate of Gd_6@PEG and Gd_6−ZnDPA was less than 5% for concentrations of [Gd] under 100 μg mL^{-1} (Figure 3a). After cocultivation with Gd_6@PEG and Gd_6−ZnDPA for 6 and 12 h, respectively, the viability of 4T1 cells displayed an acceptable trend, with the viability exceeding approximately 75% at concentrations up to 100 μg mL^{-1} for 6 and 12 h, suggesting that both Gd_6@PEG and Gd_6−ZnDPA possess a comparatively low cytotoxic effect (Figure 3b).

Additional confirmation of the targeting capability of Gd_6−ZnDPA in vitro is necessary before in vivo injection. The Gd_6−ZnDPA surface was tagged with fluorescein isothiocyanate (FITC), denoted as Gd_6−ZnDPA/FITC. Subsequently, Gd_6−ZnDPA/FITC samples were subjected to cocultivation with apoptotic 4T1 cells for 2 h. Confocal laser scanning microscopy (CLSM) was performed to observe the fluorescence images of each group. The green fluorescence in the targeting group was significant and highly overlapped with the red fluorescence area, in comparison to apoptosis and the blocking group. This indicates that Gd_6−ZnDPA/FITC (green) successfully targeted 4T1 apoptotic cells induced by DOX (red) (Figure 4a).

The red fluorescence emitted by DOX in all three groups (apoptosis, target, and blocking groups) served as the internal standard to quantify the intensity of the fluorescence. In the apoptosis group, there were only red apoptotic cells with minimal green fluorescence, and the fluorescence intensity ratio of the green to red channels was approximately 0.26. However, after coculturing Gd_6−ZnDPA/FITC with apoptotic cells in the targeting group, the intensity of green fluorescence in the field was significantly enhanced, resulting in a fluorescence intensity ratio of approximately 0.90. This is about 3 times higher than that of the apoptotic group. However, the intensity of green fluorescence was not as strong in the blocking group, with a fluorescence intensity ratio of approximately 0.29, due to the initial binding of ZnDPA to the target site—PS (Figure 4b). All of the results confirmed the great targeting behavior of Gd_6−ZnDPA toward apoptotic cells in vitro.

3.4. T_1-Weighted MRI Performance of Gd_6−ZnDPA NPs. Continuous monitoring of tumor cell apoptosis levels in chemotherapy patients may provide significant insights into the efficacy of treatment, enabling tailored therapy to optimize anticipated survival odds.[40] Gd_6−ZnDPA NPs were utilized for vein tail administration to investigate their apoptosis-targeting property in vivo. For this purpose, we divided the apoptotic 4T1 tumor model mice into two groups: a targeting group and a blocking group. Their T_1-weight images were obtained at different time points (0, 1.5, 5, 9, 24, and 48 h). We compared images from both groups and quantified their visual performance. In the targeting group, after the intravenous injection of Gd_6−ZnDPA (0.0025 mmol kg^{-1}), the tumor area became progressively brighter over time, showing significant brightness at 5 h post-injection [with a relative signal enhanced (RSE) ratio of 22.55 ± 6.90%]. This indicates that Gd_6−ZnDPA NPs were gradually accumulating in the apoptotic tumor (Figure 5a). The RSE ratio peaked at 74.22 ± 8.28% at 24 h post-injection and then gradually declined to 13.64 ± 4.42% at 48 h post-injection (Figure 5b). These results confirm the superior contrast imaging potentials of Gd_6−ZnDPA NPs and suggest a long acquisition time window of approximately 48 h. In stark contrast, mice in the blocking group were injected with the targeting motif ZnDPA (0.005 mmol kg^{-1}) for 15 min, which binds to the target site (PS) on the surface of apoptotic cells beforehand. Subsequently, they received an injection of Gd_6−

https://doi.org/10.1021/acsanm.4c00511
ACS Appl. Nano Mater. 2024, 7, 9020−9030

ZnDPA (0.0025 mmol kg^{-1}). However, it showed that the RSE ratio in the blocking group remained lower than those in the targeting group, and the T_1-weighted images were not as pronounced as in the targeting group over the entire trial period. Finally, it took 24 h for the tumor site to substantially brighten, with an RSE ratio of 17.31 ± 5.94%, followed by a decrease to 6.20 ± 4.25% at 48 h post-injection. The difference in the RSE ratio between two groups reflects the potent PS-binding ability of ZnDPA.[41] Additionally, 4T1 tumor model mice underwent T_1-weighted imaging after receiving Gd-DTPA or Gd_6−ZnDPA injections. The data collected serve as additional evaluations of the bioimaging properties of Gd_6−ZnDPA NPs. As presented in Figures 5b and S6, Gd_6−ZnDPA exhibited an extended imaging time window. Furthermore, the highest RSE ratio occurred at 1.5 h (9.01 ± 1.92%) and 5 h (12.1 ± 0.30%) in the Gd-DTPA and Gd_6−ZnDPA groups, respectively, and both converged to zero around 24 h, which demonstrated the enhanced T_1 signal value and good apoptosis-targeting ability of Gd_6−ZnDPA.

For further research, the pharmacokinetic clearance of targeted GBCAs must be taken into account.[42] The changes in signal levels of the heart, kidney, liver, and bladder in Balb/c mice were observed under a 3T MRI system after intravenous administration of Gd_6−ZnDPA NPs (Figures S7−S10). The maximum enhancement in the kidney occurred at 40 min post-injection, with an RSE ratio of 41.82% (Figure 6a,e). The peak signal intensity in the liver occurred at the 60 min mark, which was accompanied by an RSE ratio of 29.38% (Figure 6b,f). As depicted in Figure 6c,g, there was a substantial augmentation in the signal intensity of the heart (right ventricle), reaching up to 65.90%, during the time interval of 0−40 min post-injection. Then, the signal intensity in three organs (heart, kidney, and liver) gradually declined to the preinjection level at 180 min (Figure 6e−h). At 40 min after injection, both the kidney and the heart displayed the highest signal intensities, with the peak of the heart being greater than that of the kidney. This phenomenon indicated that Gd_6−ZnDPA NPs rapidly dissolved in the bloodstream following intravenous administration, with the majority being directed to the heart (right ventricle), while a small portion entered the kidneys for metabolism. At 60 min, a signal peak appeared in the liver, but the level was still lower than that in the kidney, revealing that the kidney is the primary metabolic organ for Gd_6−ZnDPA NPs. Besides, the bladder signal levels steadily increased until 180 min, reaching as high as 113.38%, suggesting the rapid blood clearance profile and desirable biosafety of Gd_6−ZnDPA NPs (Figure 6d,h).

After Gd_6−ZnDPA NPs and PBS were injected into mice, we sacrificed the mice on the 14th day, and the impacts on the heart, liver, spleen, lung, and kidney were revealed by hematoxylin and eosin (H&E) staining (Figure 7a). There was no obvious abnormal lesion in any of the sections of the five organs examined, demonstrating the safety of administering Gd_6−ZnDPA NPs to mice. In addition, a series of serum biochemical markers pertaining to liver and kidney functions were also examined, including alanine aminotransferase (ALT), aspartate aminotransferase (AST), albumin (ALB), total bilirubin (TBIL), direct bilirubin (DBIL), γ-glutamyl transpeptidase (γ-GT), urea, blood urea nitrogen (BUN), creatinine (CREA), and uric acid (UA) (Figure 7b). These findings indicate that injection of Gd_6−ZnDPA has little impact on the hepatic and renal function in mice.

4. CONCLUSIONS

In summary, our team developed Gd_6−ZnDPA nanoparticles, six-nuclei gadolinium-based nanoparticles, for the detection of tumor apoptosis in mice. Characterized by their unique multinucleus Gd(III) cluster configurations, Gd_6−ZnDPA nanoparticles exhibit a significantly enhanced signal ratio (74.22 ± 8.28%), thereby facilitating the circumvention of high-dose administrations in vivo. Furthermore, integration of the Gd_6 cluster with the ZnDPA targeting moiety helped realize an active targeting paradigm, enabling precise imaging of apoptotic tumor lesions. Considering their favorable biocompatibility and biosafety profiles, Gd_6−ZnDPA NPs demonstrate great potential as T_1-targeting contrast agents for monitoring the therapeutic responses of tumors to chemotherapeutic interventions.

■ ASSOCIATED CONTENT

Supporting Information

The Supporting Information is available free of charge at https://pubs.acs.org/doi/10.1021/acsanm.4c00511.

Thermogravimetric analysis data of the Gd_6 cluster; X-ray powder diffraction pattern (PXRD) of the Gd_6 cluster; X-ray photoelectron spectroscopy (XPS) spectra of (a) the Gd_6 cluster; transmission electron microscopy (TEM) mapping and energy-dispersive X-ray spectroscopy (EDX) spectra of Gd_6@PEG; ζ-potential distribution of Gd_6−ZnDPA nanoparticles; size distribution of Gd_6−ZnDPA nanoparticles; transmission electron microscopy (TEM) image of Gd_6−ZnDPA nanoparticles; T_1-weighted images and longitude relaxivity (r_1) of Gd_6−ZnDPA NPs; in vivo T_1-weighted images of a Balb/c mice bearing 4T1 tumors before and after intravenous administration of Gd-DTPA and Gd6-ZnDPA using a 3T scanning system; T_1-weighted images of the liver, heart, kidney, and bladder before and after intravenous administration of Gd_6−ZnDPA (0.0025 mmol/kg) to Balb/c mice using a 3T scanning system; the Solomon−Bloembergen−Morgan (SBM) theory; crystallographic parameters of the Gd_6 cluster; proportional analysis of the constituents of the two nanoparticles by ICP-AES (PDF)

■ AUTHOR INFORMATION

Corresponding Authors

Yunsheng Ma − *Key Laboratory of Advanced Functional Materials, School of Chemistry & Materials Engineering, Changshu Institute of Technology, Changshu 215500, P. R. China*; orcid.org/0000-0002-9438-1232; Email: myschem@cslg.edu.cn

Yuehua Li − *Department of Diagnostic and Interventional Radiology, Shanghai Sixth People's Hospital Affiliated to Shanghai Jiao Tong University School of Medicine, Shanghai 200233, P. R. China*; Email: liyuehua312@163.com

Wu Wang − *Department of Diagnostic and Interventional Radiology, Shanghai Sixth People's Hospital Affiliated to Shanghai Jiao Tong University School of Medicine, Shanghai 200233, P. R. China; Department of Radiology, Longhua Hospital, Shanghai University of Traditional Chinese Medicine, Shanghai 200032, P. R. China*; orcid.org/0009-0001-5036-6372; Email: wangwangwuwu@hotmail.com

https://doi.org/10.1021/acsanm.4c00511
ACS Appl. Nano Mater. 2024, 7, 9020−9030

Authors

Yufan Wu − *Department of Diagnostic and Interventional Radiology, Shanghai Sixth People's Hospital Affiliated to Shanghai Jiao Tong University School of Medicine, Shanghai 200233, P. R. China*

Shuo Zhao − *Joint International Research Laboratory of Resource Chemistry of Ministry of Education, Shanghai Key Laboratory of Rare Earth Functional Materials, and Shanghai Frontiers Science Center of Biomimetic Catalysis, Shanghai Normal University, Shanghai 200234, P. R. China*

Ye Xu − *Key Laboratory of Advanced Functional Materials, School of Chemistry & Materials Engineering, Changshu Institute of Technology, Changshu 215500, P. R. China;* orcid.org/0000-0002-4321-9657

Chaojie Tang − *Department of Diagnostic and Interventional Radiology, Shanghai Sixth People's Hospital Affiliated to Shanghai Jiao Tong University School of Medicine, Shanghai 200233, P. R. China*

Yujie Feng − *Joint International Research Laboratory of Resource Chemistry of Ministry of Education, Shanghai Key Laboratory of Rare Earth Functional Materials, and Shanghai Frontiers Science Center of Biomimetic Catalysis, Shanghai Normal University, Shanghai 200234, P. R. China*

Mianmian Zhang − *Department of Diagnostic and Interventional Radiology, Shanghai Sixth People's Hospital Affiliated to Shanghai Jiao Tong University School of Medicine, Shanghai 200233, P. R. China*

Hong Yang − *Joint International Research Laboratory of Resource Chemistry of Ministry of Education, Shanghai Key Laboratory of Rare Earth Functional Materials, and Shanghai Frontiers Science Center of Biomimetic Catalysis, Shanghai Normal University, Shanghai 200234, P. R. China;* orcid.org/0000-0003-0307-3494

Complete contact information is available at: https://pubs.acs.org/10.1021/acsanm.4c00511

Author Contributions

[⊥]Y.W. and S.Z. contributed equally to this work.

Notes

The authors declare no competing financial interest.

CCDC 2338525 contains the supplementary crystallographic data for this research. Detailed information can be obtained free of charge at 12 Union Road, Cambridge CB2 1EZ, U.K. [Fax: (Internet.) +44-1223/336-033; E-mail: deposit@ccdc.cam.ac.uk].

■ ACKNOWLEDGMENTS

The authors gratefully acknowledge financial support from the National Natural Science Foundation of China, Grant Nos 8225024 and 81871329, the Shanghai 2023 "Explorer Plan" No. 23TS1400400, and the Shanghai Key Clinical Specialty (No. shslczdzk03203).

■ REFERENCES

(1) Siegel, R. L.; Miller, K. D.; Fuchs, H. E.; Jemal, A. Cancer statistics, 2022. *Ca-Cancer J. Clin.* **2022**, *72* (1), 7−33.

(2) DeVita, V. T., Jr; Chu, E. A history of cancer chemotherapy. *Cancer Res.* **2008**, *68* (21), 8643−8653.

(3) Carneiro, B. A.; El-Deiry, W. S. Targeting apoptosis in cancer therapy. *Nat. Rev. Clin. Oncol.* **2020**, *17* (7), 395−417.

(4) Vogelzang, N. J.; Rusthoven, J. J.; Symanowski, J.; Denham, C.; Kaukel, E.; Ruffie, P.; Gatzemeier, U.; Boyer, M.; Emri, S.; Manegold, C.; et al. Phase III study of pemetrexed in combination with cisplatin versus cisplatin alone in patients with malignant pleural mesothelioma. *J. Clin. Oncol.* **2003**, *21* (14), 2636−2644.

(5) Williamson, P.; Schlegel, R. A. Transbilayer phospholipid movement and the clearance of apoptotic cells. *Biochim. Biophys. Acta, Mol. Cell Biol. Lipids* **2002**, *1585* (2−3), 53−63.

(6) Prinzen, L.; Miserus, R. J. J.; Dirksen, A.; Hackeng, T. M.; Deckers, N.; Bitsch, N. J.; Megens; Douma, K.; Heemskerk, J. W.; Kooi, M. E.; et al. Optical and magnetic resonance imaging of cell death and platelet activation using annexin A5-functionalized quantum dots. *Nano Lett.* **2007**, *7* (1), 93−100.

(7) Zhao, H.; Zhou, P.; Huang, K.; Deng, G.; Zhou, Z.; Wang, J.; Wang, M.; Zhang, Y.; Yang, H.; Yang, S. Amplifying apoptosis homing nanoplatform for tumor theranostics. *Adv. Healthcare Mater.* **2018**, *7* (14), No. 1800296.

(8) Sakuragi, T.; Nagata, S. Regulation of phospholipid distribution in the lipid bilayer by flippases and scramblases. *Nat. Rev. Mol. Cell Biol.* **2023**, *24*, 576−596.

(9) Caschera, L.; Lazzara, A.; Piergallini, L.; Ricci, D.; Tuscano, B.; Vanzulli, A. Contrast agents in diagnostic imaging: Present and future. *Pharmacol. Res.* **2016**, *110*, 65−75.

(10) Clough, T. J.; Jiang, L.; Wong, K. L.; Long, N. J. Ligand design strategies to increase stability of gadolinium-based magnetic resonance imaging contrast agents. *Nat. Commun.* **2019**, *10* (1), No. 1420.

(11) Peters, J.; Huskens, J.; Raber, D. Lanthanide induced shifts and relaxation rate enhancements. *Prog. Nucl. Magn. Reson. Spectrosc.* **1996**, *28* (3−4), 283−350.

(12) Walker, D. T.; Davenport, M. S.; McGrath, T. A.; McInnes, M. D.; Shankar, T.; Schieda, N. Breakthrough hypersensitivity reactions to gadolinium-based contrast agents and strategies to decrease subsequent reaction rates: a systematic review and meta-analysis. *Radiology* **2020**, *296* (2), 312−321.

(13) Tweedle, M. F. Alternatives to gadolinium-based contrast agents. *Invest. Radiol.* **2021**, *56* (1), 35−41.

(14) Ebenezer, O. I.; Abdul, A. L.; Fazliani, N. S.; Suzylawati, I. Gadolinium based contrast agents (GBCAs): Uniqueness, aquatic toxicity concerns, and prospective remediation. *J. Contam. Hydrol.* **2022**, *250*, No. 104057.

(15) Dekkers, I. A.; Roos, R.; van der Molen, A. J. Gadolinium retention after administration of contrast agents based on linear chelators and the recommendations of the European Medicines Agency. *Eur. Radiol.* **2018**, *28*, 1579−1584.

(16) Tweedle, M. F. Gadolinium retention in human brain, bone, and skin. *Radiology* **2021**, *300*, 570−571.

(17) Du, Y.; Qian, M.; Li, C.; Jiang, H.; Yang, Y.; Huang, R. Facile marriage of Gd3+ to polymer-coated carbon nanodots with enhanced biocompatibility for targeted MR/fluorescence imaging of glioma. *Int. J. Pharm.* **2018**, *552* (1−2), 84−90.

(18) Lu, Y.; Liang, Z.; Feng, J.; Huang, L.; Guo, S.; Yi, P.; Xiong, W.; Chen, S.; Yang, S.; Xu, Y.; et al. Facile Synthesis of Weakly Ferromagnetic Organogadolinium Macrochelates-Based T1-Weighted Magnetic Resonance Imaging Contrast Agents. *Adv. Sci.* **2023**, *10* (1), No. 2205109.

(19) Antwi-Baah, R.; Wang, Y.; Chen, X.; Yu, K. Metal-Based Nanoparticle Magnetic Resonance Imaging Contrast Agents: Classifications, Issues, and Countermeasures toward their Clinical Translation. *Adv. Mater. Interfaces* **2022**, *9* (9), No. 2101710.

(20) Sun, S. K.; Dong, L. X.; Cao, Y.; Sun, H.-R.; Yan, X.-P. Fabrication of multifunctional Gd2O3/Au hybrid nanoprobe via a one-step approach for near-infrared fluorescence and magnetic resonance multimodal imaging in vivo. *Anal. Chem.* **2013**, *85* (17), 8436−8441.

(21) Cai, W.; Zhang, Y.; Wang, J.; Wang, Z.; Tian, Y.; Liu, H.; Pan, H.; Fu, L.; Chen, W.; Wu, C.; Wang, X.; Liu, G. Engineering the surface of Gd2O3 nanoplates for improved T1-weighted magnetic resonance imaging. *Chem. Eng. J.* **2020**, *380*, No. 122473.

(22) Zheng, X. Y.; Jiang, Y. H.; Zhuang, G. L.; Liu, D. P.; Liao, H. G.; Kong, X. J.; Long, L. S.; Zheng, L. S. A gigantic molecular wheel of

{Gd140}: a new member of the molecular wheel family. *J. Am. Chem. Soc.* **2017**, *139* (50), 18178−18181.
(23) Bai, H.; Wang, Y.; Hu, Y.; Ye, D. A caspase-3-activatable bimodal probe for photoacoustic and magnetic resonance imaging of tumor apoptosis in vivo. *Biosens. Bioelectron.* **2022**, *216*, No. 114648.
(24) Zhou, Z.; Yang, L.; Gao, J.; Chen, X. Structure−relaxivity relationships of magnetic nanoparticles for magnetic resonance imaging. *Adv. Mater.* **2019**, *31* (8), No. 1804567.
(25) Tian, H.; Zhang, T.; Qin, S.; Huang, Z.; Zhou, L.; Shi, J.; Nice, E. C.; Xie, N.; Huang, C.; Shen, Z. Enhancing the therapeutic efficacy of nanoparticles for cancer treatment using versatile targeted strategies. *J. Hematol. Oncol.* **2022**, *15* (1), 1−40.
(26) Tang, X.; Xu, Y.; Ye, W.; Tang, Y.; Ma, Y.; Yuan, R. Mn (II) 2Gd(III) 3 Phosphonate as a Molecular Refrigerant. *Aust. J. Chem.* **2015**, *68* (12), 1926−1928.
(27) Jerosch-Herold, M.; Kwong, R. Y. Cardiac T1 imaging. *Top. Magn. Reson. Imaging* **2014**, *23* (1), 3.
(28) Xu, Y.; Li, C.; Wu, X.; Li, M.-X.; Ma, Y.; Yang, H.; Zeng, Q.; Sessler, J. L.; Wang, Z.-X. Sheet-like 2D manganese (IV) complex with high photothermal conversion efficiency. *J. Am. Chem. Soc.* **2022**, *144* (41), 18834−18843.
(29) Zhang, S. Y.; Wang, Z.-Y.; Gao, J.; Wang, K.; Gianolio, E.; Aime, S.; Shi, W.; Zhou, Z.; Cheng, P.; Zaworotko, M. J. A gadolinium (III) zeolite-like metal-organic-framework-based magnetic resonance thermometer. *Chem* **2019**, *5* (6), 1609−1618.
(30) Wang, Z.; He, L.; Liu, B.; Zhou, L. P.; Cai, L. X.; Hu, S. J.; Li, X. Z.; Li, Z.; Chen, T.; Li, X.; Sun, Q. F. Coordination-assembled water-soluble anionic lanthanide organic polyhedra for luminescent labeling and magnetic resonance imaging. *J. Am. Chem. Soc.* **2020**, *142* (38), 16409−16419.
(31) Cao, Y.; Sun, W.; Guo, C.; Zheng, L.; Yao, M.; Wang, Y. Rational construction of yolk−shell bimetal-modified quinonyl-rich covalent organic polymers with ultralong lithium-storage mechanism. *ACS Nano* **2022**, *16* (6), 9830−9842.
(32) Shao, X.; Yang, Y.; Liu, Y.; Yan, P.; Zhou, S.; Isimjan, T. T.; Yang, X. Oxygen vacancy-rich N-doped carbon encapsulated BiOCl-CNTs heterostructures as robust electrocatalyst synergistically promote oxygen reduction and Zn-air batteries. *J. Colloid Interface Sci.* **2022**, *607*, 826−835.
(33) Ma, Z.; Kang, S.; Ma, J.; Shao, L.; Wei, A.; Liang, C.; Gu, J.; Yang, B.; Dong, D.; Wei, L.; Ji, Z. High-performance and rapid-response electrical heaters based on ultraflexible, heat-resistant, and mechanically strong aramid nanofiber/Ag nanowire nanocomposite papers. *ACS Nano* **2019**, *13* (7), 7578−7590.
(34) Raiser, D.; Deville, J. Study of XPS photoemission of some gadolinium compounds. *J. Electron Spectrosc. Relat. Phenom.* **1991**, *57* (1), 91−97.
(35) Kim, S. S.; Britcher, L.; Kumar, S.; Griesser, H. J. XPS study of sulfur and phosphorus compounds with different oxidation states. *Sains Malays.* **2018**, *47* (8), 1913−1922.
(36) Lauffer, R. B. Paramagnetic metal complexes as water proton relaxation agents for NMR imaging: theory and design. *Chem. Rev.* **1987**, *87* (5), 901−927.
(37) Srivastava, S.; Awasthi, R.; Tripathi, D.; Rai, M. K.; Agarwal, V.; Agrawal, V.; Gajbhiye, N. S.; Gupta, R. K. Magnetic-nanoparticle-doped carbogenic nanocomposite: an effective magnetic resonance/fluorescence multimodal imaging probe. *Small* **2012**, *8* (7), 1099−1109.
(38) Caravan, P. Strategies for increasing the sensitivity of gadolinium based MRI contrast agents. *Chem. Soc. Rev.* **2006**, *35* (6), 512−523.
(39) Webber, B. C.; Payne, K. M.; Rust, L. N.; Cassino, C.; Carniato, F.; McCormick, T.; Botta, M.; Woods, M. Analysis of the Relaxometric Properties of Extremely Rapidly Exchanging Gd3+ Chelates: Lessons from a Comparison of Four Isomeric Chelates. *Inorg. Chem.* **2020**, *59* (13), 9037−9046.
(40) Jiang, Y.; Wang, H.; Wu, J.; Chen, C.; Yuan, Q.; Huang, W.; Li, T.; Xi, S.; Hu, Y.; Zhou, Z.; et al. Noninvasive imaging evaluation of tumor immune microenvironment to predict outcomes in gastric cancer. *Ann. Oncol.* **2020**, *31* (6), 760−768.
(41) Chang, W.; Fa, H.; Xiao, D.; Wang, J. Targeting phosphatidylserine for Cancer therapy: Prospects and challenges. *Theranostics* **2020**, *10* (20), 9214.
(42) Lu, Z. R.; Laney, V.; Li, Y. Targeted Contrast Agents for Magnetic Resonance Molecular Imaging of Cancer. *Acc. Chem. Res.* **2022**, *55* (19), 2833−2847.

https://doi.org/10.1021/acsanm.4c00511
ACS Appl. Nano Mater. 2024, 7, 9020−9030